Parallelization and Validation of an MHD Code for the Simulation of Self-Field MPDT Flows*

K. Sankaran†, **S.C. Jardin**‡and **E.Y. Choueiri**§
Princeton University, Princeton, New Jersey 08544

IEPC-01-127¶

October 12, 2001

Abstract

The parallelization and validation of an MHD code, that was developed for the simulation of propulsive plasma flows, are described. The physical model, along with the initial and boundary conditions imposed on the numerical solver are described. A discussion of the code structure, and a description of how it works in a parallel computing environment, are included. The results of the simulation are compared with experimental measurements in a self-field magnetoplasmadynamic thruster (MPDT). The simulation depicted a number of salient features of the flowfield. With 11 processors, the parallel code obtained the converged solution 7.5 times faster than the earlier serial code.

Nomenclature

ρ	Total mass density
$\mathbf{u}$	Velocity of the fluid
$\mathbf{B}$	Magnetic induction
$p, \bar{\bar{p}}$	Gas pressure, isotropic pressure tensor
$\bar{\bar{\mathcal{B}}}_{\mathcal{M}}$	Maxwell stress tensor
E	Electric field strength
E'	Electric field seen by the plasma
$\bar{\bar{E}}_{res}$	Resistive diffusion tensor
$\mathcal{E}$	Energy density of the plasma
$\mathbf{j}$	Current density
k_B	Boltzmann's constant
$\bar{\bar{k}}_{th}$	Thermal conductivity tensor
$k_{e,i}$	Electron/ion thermal conduction coefficient
m_e	Mass of an electron
n_e	Electron number density
T_h, T_e	Heavy species/electron temperature
η	Resistivity

1 Introduction

The goal of this paper is to demonstrate the validity of a new parallel MHD code that was developed by the authors, for the simulation of plasma flows in MPD thrusters. This code, developed based on the principles of using a conservation formulation, with characteristics-splitting, and flux-limited anti-diffusion to solve the governing equations, was introduced by the authors in ref.[1], and is described in detail in ref.[2]. In this paper, we focus on the development of a parallel version of that code, and its validation by comparing the results of its simulations with experimental measurements.

In §2, we will describe the governing equations and the physical models used in this simulation.

*Research supported by NASA-JPL's Advanced Propulsion Group.
†Graduate Student, MAE Dept.
‡Principal Research Scientist, Princeton Plasma Physics Lab; Professor, Astrophysical Sciences Dept.
§Chief Scientist at EPPDyL. Assistant Professor, MAE Dept.
¶Presented at the 27^{th} International Electric Propulsion Conference, Pasadena, CA, October 14-19, 2001.

Then, in §3 we will describe the initial and boundary conditions imposed on the solver described in ref.[2] to obtain solutions of the flowfield in self-field magnetoplasmadynamic thrusters (MPDTs). In §4, we will follow that with a discussion on the parallel computing algorithm used, and describe the code structure. In §5 we will look at the results from the simulation of plasma flows in a real thruster, and compare the results to experimental measurements. Finally, a calculation of the speedup obtained by the parallel code with respect to the old serial version of the code is presented.

2 Physical Model

The governing equations for a MHD flow problem can be written in the form [3]:

$$\frac{\partial}{\partial t}\begin{bmatrix}\rho\\ \rho\mathbf{u}\\ \mathbf{B}\\ \mathcal{E}\end{bmatrix}+\nabla\cdot\begin{bmatrix}\rho\mathbf{u}\\ \rho\mathbf{uu}+\bar{\bar{p}}-\bar{\bar{\mathcal{B}}}_M\\ \mathbf{uB}-\mathbf{Bu}\\ (\mathcal{E}+p)\,\mathbf{u}-\bar{\bar{\mathcal{B}}}_M\cdot\mathbf{u}\end{bmatrix}=\mathbf{S}. \quad (1)$$

The right hand side of the equation, $\mathbf{S}$, contains the dissipative effects that are physical in nature,

$$\mathbf{S}=\nabla\cdot\begin{bmatrix}0\\ 0\\ \bar{\bar{E}}_{res}\\ \mathbf{q}\end{bmatrix}. \quad (2)$$

The energy equation is written in terms of the energy density (energy per unit volume), $\mathcal{E}$, which includes the internal energy, kinetic energy and the energy in the magnetic field.

The dissipative flux of energy, $\nabla\cdot\mathbf{q}$, contains the Ohmic heating (written in terms of divergence of the Poynting flux), and thermal conduction,

$$\nabla\cdot\mathbf{q}=\nabla\cdot\left[\frac{\mathbf{B}\times\mathbf{E}'}{\mu_0}+\bar{\bar{k}}_{th}\cdot\nabla T\right].$$

In addition to the total energy equation, separate species energy equations are needed to account for the disparity between electron and ion temperatures. The conservation relations for the internal energy density of electrons, $\mathcal{E}_e$, can be written as,

$$\frac{\partial\mathcal{E}_e}{\partial t}+\nabla\cdot[\mathcal{E}_e\mathbf{u}]+p_e\nabla\cdot\mathbf{u}=\eta j^2-\Delta\dot{\mathcal{E}}_{ie}+\nabla\cdot(k_e\nabla T_e)\ , \quad (3)$$

and that of ions, $\mathcal{E}_i$, as,

$$\frac{\partial\mathcal{E}_i}{\partial t}+\nabla\cdot[\mathcal{E}_i\mathbf{u}]+p_i\nabla\cdot\mathbf{u}=\Delta\dot{\mathcal{E}}_{ie}+\nabla\cdot(k_i\nabla T_i)\ . \quad (4)$$

In the above expressions, p_e and p_i are the pressures of the electron and heavy species respectively, and ηj^2 is the Ohmic heating term, and $\Delta\dot{\mathcal{E}}_{ie}$ is the energy exchange term to be discussed later.

Since experimental data suggest that the disparity between the two temperatures is less than an order of magnitude, only one of eqns.(3) and (4) is needed. We have verified that the internal energy of the other species can be obtained, without significant error, by subtraction from the total energy.

In eqns.(3) and (4), the rate of exchange of energy per unit volume between the electrons and the ions, through collisions, can be estimated as,

$$\Delta\dot{\mathcal{E}}_{ie}=\frac{3\rho_e\nu_{ei}}{M_i}k_B\left(T_e-T_i\right)\ , \quad (5)$$

where ρ_e is the electron mass density, and ν_{ei} is the average collision frequency between electrons and ions. Energy losses due to radiation are important in many types of plasmas. However, earlier work by Boyle[4], Villani[5], and Bruckner[6] suggests that the relative magnitude of this sink is not significant. Consequently, radiation losses will be ignored in the current model.

2.1 Ionization Processes

The plasma in a self-field, quasi-steady MPDT is generally in a state of ionizational nonequilibrium [7]. Though some numerical simulations (such as refs.[8, 9]) have used finite-rate ionization models, they do not include higher levels of ionization that have been observed experimentally [6, 10]. In the present work, like in refs.[11, 12], we use a multi-level equilibrium ionization model. Although many of these simulations depict some of the main features of the flowfield, the validity of this assumption remains to be verified. In equilibrium, irrespective of the manner in which the species are created, the

Table 1: Energy levels and statistical weights in argon and argon ions (obtained from refs. [13], [10] and [14])

Ar I		Ar II		Ar III		Ar IV	
E_l^0 (eV)	g_l^0	E_l^+ (eV)	g_l^+	E_l^{++} (eV)	g_l^{++}	E_l^{+++} (eV)	g_l^{+++}
0.000	1	0.059	6	0.111	29	0.000	4
11.577	8	13.476	2	1.737	6	3.478	16
11.802	4	16.420	20	4.124	2	14.671	24
13.096	24	16.702	12	14.214	6	31.133	24
13.319	12	17.177	6	17.856	1	35.568	40
14.019	48	17.688	28	17.964	10		
14.242	24	18.016	6	19.460	14		
14.509	24	18.300	12	20.066	1		
14.690	12	18.438	10	20.222	8		

densities of the electrons, n_e, ions, n_i, and the neutrals , n_o, are related by the Saha[15] equation,

$$\frac{n_i n_e}{n_{i-1}} = \frac{2\left(2\pi m_e k_B T\right)^{3/2}}{h^3} \frac{\sum_l g_l^i \; e^{-\epsilon_l^i/k_B T}}{\sum_l g_l^{i-1} \; e^{-\epsilon_l^{i-1}/k_B T}} = K_i \; , \tag{6}$$

where ϵ_l^i is the l^{th} energy level of the species of ionization level i, and g_l^i is the corresponding statistical weight.

Similar expressions can be written for higher ionization levels, with the energy levels scaled to a common ground. The propellant considered in this work is argon, due to the existence of wide experimental data with that propellant. The first, second and third ionization potentials of argon are 15.755 eV, 27.63 eV, and 40.90 eV respectively. The relevant energy levels of argon atom and its ions, and their statistical weights are given in Table (1).

Even in the presence of thermal nonequilibrium between electrons and ions, a modified Saha equation can be applicable. As shown in refs.[16] and [17], in such situations, due to the high mobility of the electrons, the temperature in eqn.(6) can be replaced with the temperature of the electron fluid, and the resulting modified Saha equation is an accurate model.

For a model with *N* levels of ionization, the electron number density can be obtained by finding the single positive root of the polynomial (from Heiermann[18]),

$$n_e^{N+1} + \sum_{l=1}^{N} \left[n_e^{N-l} \left(n_e - l n_o\right) \prod_{m=1}^{l} K_m \right] = 0 \; ,$$

where n_o is the total number density of all nuclei, and the equilibrium constant, K_m is from eqn.(6).

2.2 Equation of State

For monatomic propellants, the relationship between pressure, density and temperature is of the form[19]

$$p = N k_B T \frac{\partial \ln Q_{el}}{\partial V} \; . \tag{8}$$

The partition functions for many elements of interest can be found in references, such as ref.[20]. Based on this work, Choueiri[21] derived expressions to obtain the temperature from pressure and density, for argon. As shown in Fig.(1), it is clear that at temperatures above 10^4K, the deviations from the ideal gas model are significant.

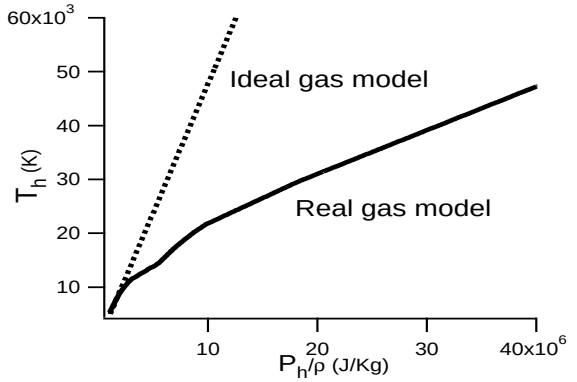

Figure 1: Deviation from ideal gas behavior for argon (calculated from data in ref.[20])

As energy is deposited into the internal modes, the ratio of specific heats also changes. Once again, this can be calculated from the partition functions. As seen in Fig.(2), the deviation from the ideal value of $5/3$ is severe at temperatures above 10^4K, which is consistent with Fig.(1).

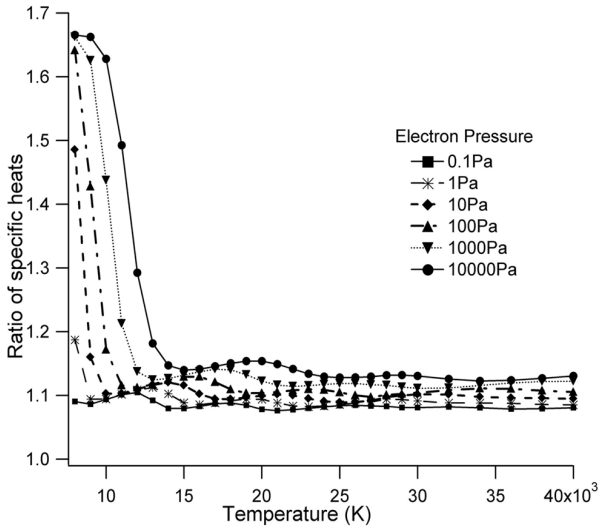

Figure 2: Variation of the ratio of specific heats for argon (calculated from data in ref.[20])

2.3 Transport Phenomena

The transport coefficients in our model are electron and ion thermal conduction, classical electrical resistivity with Hall effect and ∇p effects, and anomalous transport due to momentum exchange between microinstability induced waves and particles in the plasma. Effects of viscosity are not currently in our model. Detailed expressions for these coefficients will be given below.

2.3.1 Classical Transport

Our method for the calculation of classical transport coefficients relies on momentum transfer during elastic collisions. The energy-weighted average of the momentum transfer collision frequency between the electrons and species *s*, is given by (cf. refs.[22, 18]),

$$\nu_{es} = n_s Q_{es} \sqrt{\frac{8 k_B T_e}{\pi m_e}} \, . \tag{9}$$

If the species in consideration is an ion of charge *q*, then,

$$Q_{eq} = \frac{\pi}{4} \left(\frac{Z_q e^2}{4\pi\epsilon_o k_B T_e} \right)^2 \ln \left(1 + \frac{144\pi^2 \left(\epsilon_o k_B T_e\right)^3}{n_e e^6 Z_{eff}^2 \left(Z_{eff}+1\right)} \right) \, . \tag{10}$$

The electron-neutral collision cross section for argon is $Q_{eo} \simeq 4.0 \times 10^{-20}\mathrm{m}^2$, and the ion-neutral collision cross section is $Q_{io} \simeq 1.4 \times 10^{-18}\mathrm{m}^2$. The ion-ion collision frequency is estimated by[22]

$$Q_{ii} = \frac{5.845 \times 10^{-10}}{T_h^2} \ln 1.239 \times 10^7 \sqrt{\frac{T_h^3}{n_e}} \, . \tag{11}$$

From the abovementioned relations for collision frequencies, the coefficient for the electron thermal conductivity can be estimated as

$$k_e = 3.20 \frac{k_B^2 n_e T_e}{m_e \sum_s \nu_{es}} \, , \tag{12}$$

while that of the ions is

$$k_i = \sqrt{\frac{\pi k_B^3 T_h}{8 M_i}} \left(\frac{n_i}{n_i Q_{ii} + n_o Q_{io}} \right) \, . \tag{13}$$

The electrical resistivity is defined as

$$\eta_o \equiv \frac{m_e \sum_s \nu_{es}}{n_e e^2} \,, \tag{14}$$

and the electron Hall parameter is

$$\Omega_e = \frac{\omega_{c,e}}{\sum_s \nu_{es}} = \frac{eB/m_e}{\sum_s \nu_{es}} \,. \tag{15}$$

2.3.2 Anomalous Transport

It is known that the current can drive microinstabilities in the thruster plasma which may, through induced microturbulence, substantially increase dissipation and adversely impact the efficiency. The presence of microinstabilities in such accelerator plasmas has been established experimentally in the plasma of the MPDT at both low and high power levels[23], [24]. Choueiri[25] has developed a model to estimate the resulting anomalous transport and heating in terms of macroscopic parameters. Under this formulation, apart from the classical collision frequency of the particles, there exists additional momentum and energy transferring collisions between particles and waves. The resulting anomalous collision frequency is important whenever the ratio of electron drift velocity to ion thermal velocity, $u_{de}/v_{ti} \geq 1.5$. Above this threshold, the ratio of anomalous collision frequency to classical collision frequency was found to depend on the classical electron Hall parameter, Ω_e, and the ratio of ion to electron temperatures, T_i/T_e. A polynomial expression for the ratio of anomalous to classical collision frequencies was derived in ref.[25] to be,

$$\begin{aligned}\frac{\nu_{e_{an}}}{\nu_{e_{cl}}} = \big(0.192 + 3.33 \times 10^{-2}\Omega_e + 0.212\Omega_e^2 \\ -8.27 \times 10^{-5}\Omega_e^3\big) + \frac{T_h}{T_e}\big(1.23 \times 10^{-3} \\ -1.58 \times 10^{-2}\Omega_e - 7.89 \times 10^{-3}\Omega_e^3\big) \,,\end{aligned} \tag{16}$$

where $\nu_{e_{cl}}$ is the classical electron collision frequency computed in eqn.(9), and $\nu_{e_{an}}$ is its anomalous counterpart representing the momentum exchange between electrons and microturbulence fluctuations.

As a result, the effective resistivity of the plasma can be expressed as

$$\eta_{\text{eff}} = \frac{m_e\left(\nu_{e_{cl}} + \nu_{e_{an}}\right)}{e^2 n_e} \,. \tag{17}$$

3 Numerical Solution

The techniques for the numerical solution of eqns.(1-3) are described in ref.[2], and in this section we will only describe the initial and boundary conditions imposed on that solver, to obtain solution for the flowfield in a self-field MPDT.

3.1 Boundary Conditions

The set of governing equations (eqns.(1-3)) describe the evolution of many types of drastically different plasma flows. It is the role of the boundary conditions to distinguish one problem from another. This section will discuss the estimation of the convective and dissipative terms at various boundaries.

3.1.1 Flow Properties

Free Stream

The computational domain is taken to be large enough (seven exit radii downstream of anode tip) such that there are no normal gradients in any of the flow properties at the free stream boundaries.

Solid Walls

The governing equations require the value of thermal conduction between the wall and the plasma to be specified. This can either be given explicitly (as in the case of adiabatic walls, for which thermal conduction is zero), or can be computed by fixing the temperature of the wall. In this simulation, the thermal conduction is set to zero at insulators, and the wall temperature is set to 2500 K at metallic boundaries, consistent with experimental data (cf.[26]), as well as other simulations (cf.[12]).

Centerline

At the axis of symmetry, there are no radial convective fluxes. Moreover, there are no radial gradients. Therefore, there is no thermal conduction across the centerline.

Inlet

At the inlet, a specified mass flow rate of the propellant enters at a specified temperature at sonic conditions. In reality, the propellant is injected as neutral gas at room temperature, and it gets almost fully ionized within a few millimeters from the inlet[10]. However, it is believed[27] that this ionization process cannot be modeled by fluid theory. Therefore, in this model, the inlet temperature is chosen to be high enough such that the propellant is sufficiently ionized. Effectively, the backplate of the numerical model is not the true backplate, but a region located few millimeters downstream of it.

On this issue, our simulation distinctly differs from that of ref.[12], and ref.[28]. In both these simulations, the propellant is injected at close to room temperatures, and ionization is allowed to develop in a classical fashion. Therefore, in both ref.[12] and [28], the plasma is only weakly ionized through most of the thruster channel. However, experimental measurements [10, 29] show that the propellant is fully ionized upstream in the channel. Therefore, in our simulation, the plasma is set to be fully ionized at the inlet.

3.1.2 Field Properties

Free Stream

The computational domain is chosen to be large enough such that all the current is enclosed within the domain. Thus, from Ampère's law, the magnetic field at the free stream boundaries is zero.

Solid Walls

At all other boundaries, the magnetic field is computed from Faraday's law, which through Stokes' theorem, can be written as,

$$\int_A \frac{\partial \mathbf{B}}{\partial t} \cdot d\mathbf{A} = -\oint_C \mathbf{E} \cdot d\mathbf{l} \; . \tag{18}$$

In the cell-centered scheme used in this work, eqn.(18) implies that the evolution of the magnetic flux is specified by the contour integral of the electric field around a cell. Therefore, the only information required is the electric field drop along the boundaries.

From classical electromagnetic theory[30], the jump in the magnetic field, $\mathbf{H}_2 - \mathbf{H}_1$, across an interface between two media has to satisfy the relation,

$$\hat{\mathbf{n}} \times (\mathbf{H}_2 - \mathbf{H}_1) = \mathbf{J}_s \; , \tag{19}$$

where $\mathbf{J}_s$ is the surface current per unit length, and $\mathbf{n}$ is the unit vector normal to the surface. Due to the no mass flux condition, the potential drop at a wall is entirely resistive, and is given by,

$$\mathbf{E}_w = \eta_w \mathbf{j}_w \; . \tag{20}$$

At conducting boundaries, all the current entering the discharge flows at the surface, at least in the transient case. Therefore, even though resistivity, η_w, for most conductors is very small compared to the plasma resistivity,

$$\begin{array}{ll} \eta_{\text{plasma}} & \sim \mathcal{O}\left(10^{-3} - 10^{-4}\right) \text{ Ohm.m} \; , \\ \eta_{\text{tungsten}} & = 5.6 \times 10^{-8} \text{ Ohm.m} \; , \end{array} \tag{21}$$

the surface electric field is significant, due to the large current density in the transient case. In a true steady state, after the magnetic field has diffused into the conductor, the surface potential drop decreases to zero.

At insulated boundaries, the magnetic field diffuses into the wall instantaneously. Therefore, the jump in the magnetic field, and subsequently the surface current, is zero.

Centerline

Due to symmetry, the inductive component of the electric field is zero, because there is no flow across it. However, the resistive component is finite. This can be obtained from the value of the magnetic field at a point close to $r = 0$, through a simple Taylor series expansion [3],

$$E_z|_{r=0} = E_z'|_{r=0} = \eta j_z|_{r=0} = \eta \frac{4 \; B_\theta|_{\Delta r/2}}{\mu_o \Delta r} \; . \tag{22}$$

Inlet

Since all the enclosed current is downstream of the inlet (the backplate), the streamfunction, $\psi = r B_\theta = \mu_o J_{tot}/2\pi$ is a constant at any given time, as it depends only on the total current. The electric field

along the backplate, required for Faraday's law, is

$$E_r(r,0) = E_r(r,\Delta z) + \Delta z \left(\frac{1}{r}\frac{\partial \psi}{\partial t} - \frac{\partial E_z}{\partial r} \right) . \quad (23)$$

3.2 Initial Conditions

The governing equations (eqns.(1-3)) are time dependent in nature, and require that the initial spatial distribution of the quantities be prescribed. However, in this work, we are interested only in the steady state results. The time-dependent solutions obtained during convergence to steady state are not to be taken as representative of the evolution of the discharge.

The code is typically started with the entire domain filled with a background pressure of 10^{-4} Torr at a temperature of 300 K. Then, the inlet boundary conditions, corresponding to a fully ionized plasma entering at a specified mass flow rate, are imposed. After the plasma has filled the thrust chamber, magnetic field effects are introduced by increasing the total current in the domain. For the calculations shown in §5, the total current was increased from 0 to 15 kA in $\sim 5\mu$s.

Until this moment, the ionization is frozen at Z=1, and the ratio of specific heats is fixed at $\gamma = 5/3$. After the current has permeated the thrust chamber, the effects of multi-level equilibrium ionization and non-ideal equation of state are slowly introduced. For instance, let γ^* be the calculated value of γ at a time level $n+1$, and γ^n be the old value at time level n. Then, the value of γ used at time level $n+1$ is:

$$\gamma^{n+1} = \{\alpha\gamma^*\} + \{(1-\alpha)\,\gamma^n\} \ , \quad (24)$$

where α is a relaxation parameter between 0 and 1. A similar method is used for introducing ionization effects. This sort of "relaxation" is helpful in making the transition from an unphysical initial condition to a more realistic flowfield.

3.3 Temporal Discretization

Unlike in neutral fluid mechanics, the equations of MHD allow many different types of waves to exist. Even though physically the flow velocity is the sought quantity of most interest to propulsion, numerically the velocity of the fastest wave is what determines the constraints on time stepping. In plasmas of propulsion interest, the fluid velocity is $\mathcal{O}(10^4)$ m/s. For a quasineutral plasma with a charge density of $\mathcal{O}(10^{21})/\mathrm{m}^3$, a thermodynamic pressure of $\mathcal{O}(10^{-1})$ Torr, and a magnetic pressure of $\mathcal{O}(10^1)$ Torr, the fast magnetosonic wave speed is typically of the same order of magnitude as the flow velocity. This indicates that an explicit time marching scheme is suitable. From the CFL criterion[31], the time step for such a problem (with $\Delta r \simeq 1$mm) would be $\mathcal{O}(10^{-8} - 10^{-9})$ s.

Physical dissipation brings in different characteristic time scales into the problem. They are:

$$\text{Magnetic diffusion} = \frac{\mu_o \Delta r^2}{\eta} \sim 10^{-10} \text{ s} \ ,$$

$$\text{Heat conduction} = \frac{n_e k_B \Delta r^2}{k_e} \sim 10^{-10} - 10^{-11} \text{ s} \ .$$

As a result of this disparity in time scales, a time-accurate simulation to steady state ($\sim 200\mu$s) would require about 2×10^6 time steps, and would take about 2 weeks of CPU time (on a Pentium-II 450 MHz machine). In order to make this code a more amenable tool for research, this time has to be reduced to ≤ 1 day. Two different means of achieving this can be identified:

1. instead of treating all the terms explicitly, treat the time-limiting dissipative terms implicitly: this allows a larger time step (closer to the convective time scale) to be used for computation,

2. increase the computational power that is available for calculation, by using more than one processor to perform the computations.

In this paper, we will discuss the latter approach, whilst the former will be a topic of future work.

3.4 Spatial Discretization

Mathematically, the governing equations (eqns.(1-3)) are mixed hyperbolic and parabolic partial differential equations. We use standard central differencing schemes for the discretization of parabolic terms. For the hyperbolic terms, the fluxes in and out of

a cell boundary are estimated using characteristics splitting techniques, combined with flux-limited anti diffusion. These principles are explained in ref.[2] in detail.

Since the goal of this paper is to demonstrate the validity of the newly parallelized code, only a simple structured orthogonal grid is used here.

4 Parallelization

With the current trend in high performance computer architectures being away from single processor scalar/vector machines, and toward the design and construction of parallel machines, it is important to exploit the strength of parallel computing platforms (cf. ref[32]). For a given multiprocessor architecture, two distinct means of utilizing the computational power to solve a given problem can be identified: process decomposition, and domain decomposition[33].

Process decomposition is the allocation of specific processors to specific portions of the algorithm. For instance, for the problem at hand, the ionization model can be computed by one processor, the equation of state model by another, the convective and diffusive fluxes by another, and so on. This is the preferred choice of processor allocation under the Parallel Virtual Machine (PVM) method of parallel computing[33]. However, this method would encounter serious difficulties if the computer memory were distributed across various processors (as it is in the case of the machine we are using: the SGI Origin 2000 system). Moreover, there are difficulties in ensuring that all the processors are utilized continuously, and in transporting the code across systems with different number of processors.

Due to the abovementioned difficulties, we have chosen to follow the domain decomposition method of parallel computing. In this technique, the domain is divided into smaller domains, and these smaller domains are assigned to each of the available processors. Each processor only computes the solution in the domain it is assigned. If the domain of each processor is roughly of the same size, then all processors will finish one time step at roughly the same time, and if necessary, communicate with each other about the updated solution. This feature, often termed as "load balancing" ensures maximum utilization of the available computing power. Moreover, with domain decomposition, transporting the code across computers with varying number of processors is a relatively easy task.

Under domain decomposition, in order to estimate the values at time *t* near the boundaries, processors require knowledge of variables (at time $t - \Delta t$) that lie just outside the boundaries of their domain. Under the current discretization scheme, each processor needs exactly one row of cells from each of its neighboring processor's domain, as illustrated in Fig.(4). In this work, we use the Message Passing Interface (MPI) standard [34] to handle these interprocessor communications.

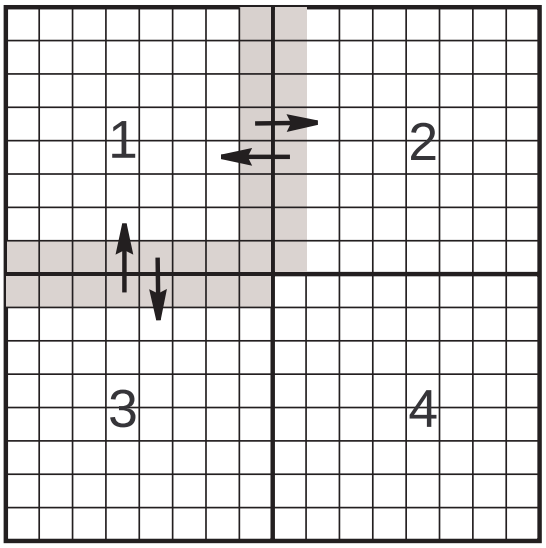

Figure 3: Information sent and received by a processor

There are certain parts of the code (such as input/output, convergence checks, and estimating global time steps) that are not amenable to parallelization. This constitutes an overhead, and we assign a separate processor (termed MASTER) to handle this. All the other processors (termed WORKERS) are exclusively involved in computation of the solution within their assigned domains, or are communicating with other processors for this purpose. The schematic of the calculations in our code is

shown in Fig.(4).

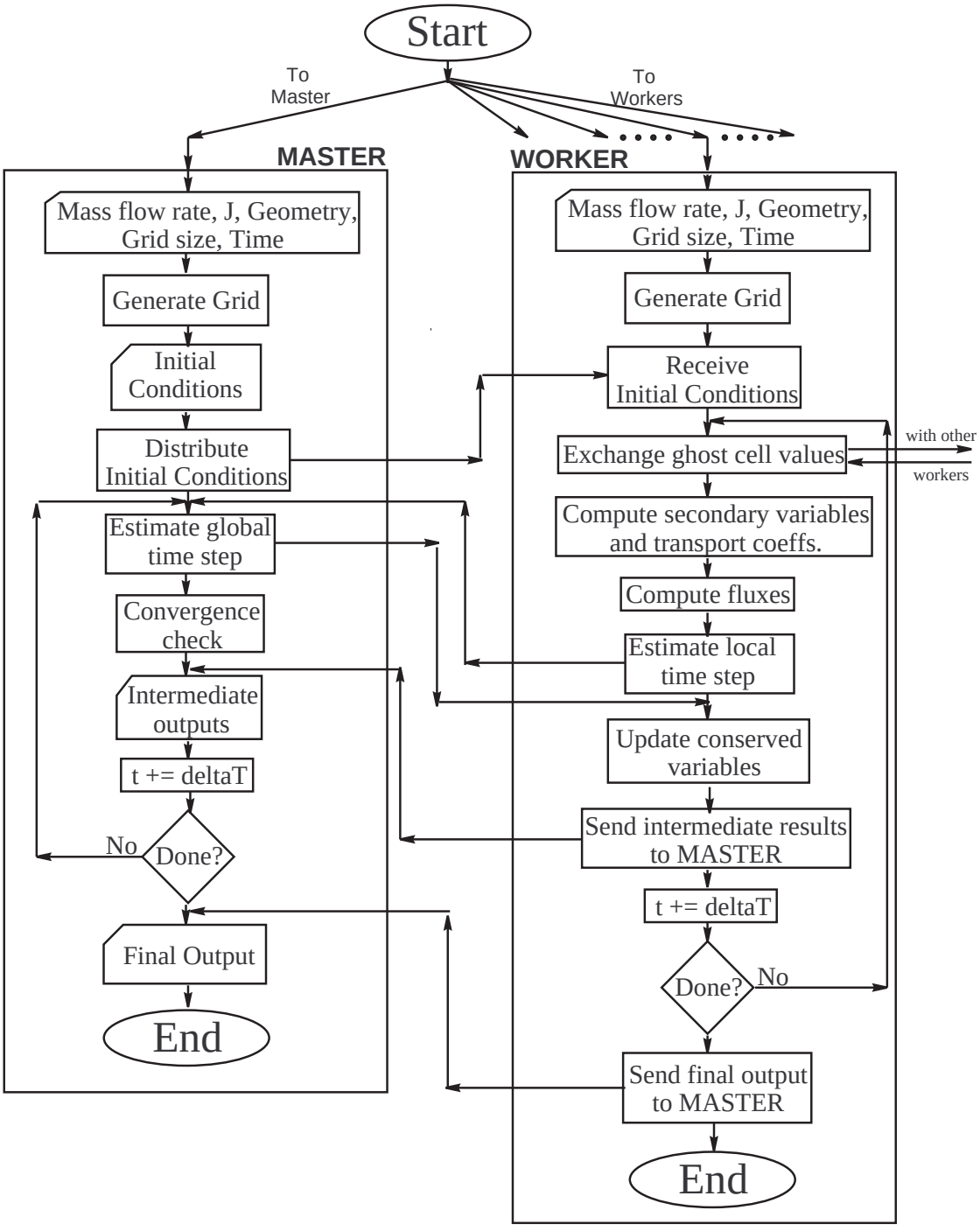

Figure 4: Flow chart of the parallel MHD code

4.1 Parallelization Results

In order to verify the effectiveness of the MPI algorithm with domain decomposition for parallelization, the 2-D heat diffusion heat equation

$$\frac{\partial T}{\partial t} = \nabla^2 T \ , \tag{25}$$

was solved on a 500 $\times$ 500 grid. This domain was decomposed into several parts, and the speed up from a single processor calculated was noted. The results from these tests are shown in Table (2).

Then, the problem at hand, the simulation of plasma flows in a MPDT, was run with 11 processors. This parallelized code was 7.5 faster than our serial code, for the same problem. The comparison of this speedup with the speedup of the heat diffusion equation is shown in Table (2).

Table 2: Parallelization

# CPUs	Heat eqn.	MPDT
4	3.8	?
11	10.5	7.5
20	17	?
30	22	?
64	30	?

5 MPDT Simulation Results

The geometry chosen for this simulation was one of the series of constant area coaxial thrusters, used by Villani[5]. We chose such a constant area thruster due to its simplicity and the availability of current contours and floating potential data. In this particular case, the cathode and the anode radii were 0.95 cm and 5.10 cm respectively. The cathode and the anode lengths were 26.4 cm and 20.0 cm respectively. The propellant mass flow rate is 6.0g/s of argon, and the total current was 15.0 kA.

In this section, we present some of the results of the simulation. Because of the simple grid adapted here (structured orthogonal), the rounded corners of the anode, and the tip of the cathode, are represented as a sharp corner, and a flat tip, respectively, in the simulation.

In order to verify convergence, the maximum and average *value*, and the maximum and average *change* of the conserved variables (mass, momentum, energy, and magnetic field) were monitored. The criterion used for establishing convergence was that the average change be less than 10^{-7}.

5.1 Density

The electron number density contours within the chamber are shown in Fig.(8), where we note that n_e increases from the anode to the cathode. This may be attributed to the radial pumping force, $j_z B_\theta$, which pushes the plasma away from the anode, towards the centerline. This trend has been observed in experiments and in previous simulations[8].

5.2 Ionization Levels

The effective ionization fraction is shown in Fig.(9). The presence of Ar-III and a small amount of Ar-IV in the plume is in agreement with experimental observations (cf. ref.[6]) for these operating conditions.

5.3 Velocities

The contours of axial velocities in the domain are shown in Fig.(10). They fall in the range of measured values of local velocities reported in ref.[35], for an operation of an MPDT with a different geometry, but same operating conditions.

The velocity streamlines (where the velocity vector is a tangent at every point) are plotted in Fig.(7), and show the increase in the radial component of velocity that occurs downstream of the anode.

5.4 Enclosed Current and Electric Potential

The contours of enclosed current are shown in Fig.(5). The calculated values are in general agreement with the measurements within the thruster chamber. The convection of the current lines beyond the anode exit plane, in the simulation, are somewhat less than that observed by experiments. This may be because of possible current attachment in the outer

surface of the anode in the experiment, which is precluded in the simulation. This could be also due to some details of the physical models, or may also be influenced by the artificially high value of the electric field at the sharp corner of the anode.

In this simulation, we did not have a model for the sheath voltage drop. This simulation predicts a voltage drop across the plasma of 30.83 Volts (cf. Fig.(6)). The true voltage drop is 56 Volts [5], and the difference can be attributed to the 25 Volts of anode drop that was indeed measured. To aid comparison with measurement, the calculated potential contours were shifted by that amount. These contours are shown in Fig.(6), where a generally good agreement can be noted.

5.5 Thrust & Efficiency

By definition, the thrust is computed using the following relation,

$$T = \int_A u_z \left(\rho \mathbf{u} \cdot d\mathbf{A}\right) \ , \tag{26}$$

where the integral is performed over all the boundaries. Using eqn.(26), the code predicts a thrust of 42.9 N. Although no thrust measurement exists for this geometry, it is well known[36] that the thrust of self-field MPDTs operating in a overwhelmingly electromagnetic acceleration regime, can be estimated by the Maecker's law

$$T = \frac{\mu_o}{4\pi}\left(\ln\frac{r_a}{r_c} + A\right) J^2, \tag{27}$$

where A is a dimensionless constant, estimated to be 0.15[5]. For the present case, eqn.(27) predicts a thrust of 41.2 N.

With the calculated value of potential difference (30.83 Volts), and the measure anode fall (25 Volts), the thrust efficiency (which was not measured) was calculated to be 18.3%.

6 Concluding Remarks

In this paper, we described the parallelization of our MHD code that was developed for the simulation of propulsive plasma flows. We discuss the physical models: the two-temperature MHD equations, with suitable transport properties, ionization and equation of state models. We discuss the techniques for obtaining a numerical solution of the governing equations, with specific emphasis on the initial and boundary conditions.

We discussed the functioning of the code in a parallel computing environment. Specifically, we describe the domain decomposition technique, with MPI based parallel computing, that was used to utilize multiple processors. By this method, we cut down the time required for simulation by a factor of 7.5 over our serial code, by using 11 processors (10 workers + 1 master). Further investigation into parallel computing techniques could improve the efficiency of the speedup even more.

To validate this code, we compared the results of the simulation with experimental measurements in a quasi-steady, self-field MPDT. The results of the simulation were in general agreement with measurements for many quantities, including species densities, velocities, current and potential contours. The value of thrust predicted by the simulation was in good agreement with the result from Maecker's law.

References

[1] K. Sankaran and E.Y. Choueiri. An accurate characteristics-splitting scheme for numerical solution of MHD equations. *IEPC-99-208*, 1999.

[2] K. Sankaran, L. Martinelli, S.C. Jardin, and E.Y. Choueiri. A flux-limited numerical method for the MHD equations to simulate propulsive plasma flows. *Int. J. Num. Meth. Eng. (accepted for publication)*, 35, 2002.

[3] K. Sankaran. Simulation of MPD Flows Using a Flux-Limited Numerical Method for the MHD Equations. Master's thesis, Princeton University, 2001.

[4] M. J. Boyle. *Acceleration Processes in the Quasi-Steady Magnetoplasmadynamic Discharge*. PhD thesis, Princeton U., 1974.

[5] D. D. Villani. *Energy Loss Mechanisms in a Magnetoplasmadynamic Arcjet*. PhD thesis, Princeton U., 1982.

[6] A. P. Bruckner. *Spectroscopic Studies of the Exhaust Plume of a Quasi-Steady MPD Accelerator*. PhD thesis, Princeton U., 1972.

[7] E. J. Sheppard. *Ionization Nonequilibrium and Ignition in Self-Field Magnetoplasmadynamic Thrusters*. PhD thesis, MIT, 1992.

[8] E. H. Niewood. *An Explanation for Anode Voltage Drops in an MPD*. PhD thesis, MIT, 1993.

[9] G. Caldo. Numerical simulation of MPD thruster flows with anomalous transport. Master's thesis, Princeton University, 1994.

[10] T. M. Randolph. Measurement of Ionization Levels in the Interelectrode Region of an MPD Thruster. Master's thesis, Princeton University, 1994.

[11] H. O. Schrade, P. C. Sleziona, T. Wegmann, and H. L. Kurtz. Basic processes of plasma propulsion: Final report. *AFOSR: 91-0118*, 1991.

[12] M.R. LaPointe and P.G. Mikellides. High Power MPD Thruster Development at the NASA Glenn Research Center. *AIAA-01-3499*, 2001.

[13] J. Vlcek. A collisional-radiative model applicable to argon discharges over a wide range of conditions: Formulation and basic data. *J. Phys.D*, 22:623, 1988.

[14] V. Kaufmann and W. Whaling. Improved wavelengths and energy levels of doubly-ionized argon (ar iii). *J. Res. Natl. Inst. Stand. Technol.*, 101:691, 1996.

[15] M. N. Saha. Ionization in the solar chromosphere. *Phil. Mag.*, 40:472, 1920.

[16] J. L. Kerrebrock and M. A. Hoffman. Nonequilibrium ionization due to electron heating. *AIAA J.*, 2:1072, 1964.

[17] S. Suckewer. Excitation and ionization of atoms and ions in a non-thermal plasma. II: Ionization equilibrium. *J. Phys. B*, 3:390–398, 1970.

[18] J. Heiermann, M.Auweter-Kurtz, and P.C. Sleziona. Adaptive computation of the current-carrying plasma in an MPD rocket thruster. *Time-Dependent Magnetohydrodynamics: Anayltical, Numerical, and Application Aspects*, 1998.

[19] C. L. Tien and J. H. Lienhard. *Statistical Thermodynamics*. Holt Rinehart Winston, Inc., 1971.

[20] W. M. Sparks and D. Fischel. *Partition Functions and Equations of State in Plasmas*. NASA SP-3066, 1971.

[21] E. Y. Choueiri. A Scaling Strategy for the Preliminary Design of MPD Thrusters. Master's thesis, Syracuse University, 1983.

[22] M. Mitchner and C.H. Kruger. *Partially Ionized Gases*. Willy-Interscience, 1973.

[23] E.Y. Choueiri, A. J. Kelly, and R.G. Jahn. Current-driven plasma acceleration versus current-driven energy dissipation: Part ii: Electromagnetic wave stability theory and experiments. *IEPC-91-100*, 1991.

[24] D.L. Tilley, E.Y. Choueiri, A. J. Kelly, and R.G. Jahn. Microinstabilities in a 10-kilowatt self-field magnetoplasmadynamic thruster. *J.Prop.Power*, 12(2):381, 1996.

[25] E.Y. Choueiri. Anomalous resistivity and heating in current-driven plasma thrusters. *Phys. Plasmas*, 6(5):2290, 1999.

[26] G. Popov, V. Kim, V. Tikhonov, S. Semenikhin, and M. Tibrina. The fourth (final) quarterly report on the milestones. *NASA-JPL-960938*, 1998.

[27] E.Y. Choueiri and H. Okuda. Anomalous ionization in MPD thrusters. *IEPC-93-067*, 1993.

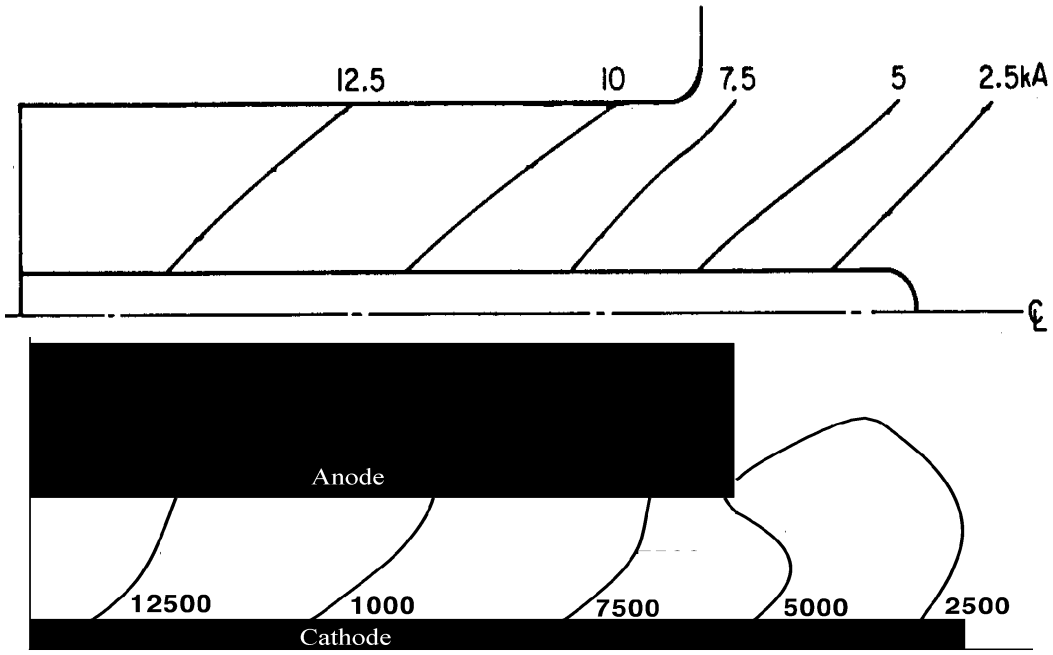

Figure 5: Measured (top) and calculated (bottom) current contours

[28] J. Heiermann and M. Auweter-Kurtz. Numerical and experimental investigation of the current distribution in self-field MPD thrusters. *AIAA-01-3498*, 2001.

[29] V. A. Abramov et al. Investigation of electron temperature and plasma radiation in a quasi-steady high-current discharge between coaxial electrodes. *Proceedings of the 8th International Conference on Phenomena in Ionized Gases*, 1968.

[30] J.D. Jackson. *Classical Electrodynamics*. Wiley, 1975.

[31] C. B. Laney. *Computational Gasdynamics*. Cambrigde, 1998.

[32] U. Shumlak. Development of an advanced implicit algorithm for MHD computations on parallel supercomputers. *AFRL-SR-BL-TR-00-0654*, 1999.

[33] S. G. Sheffer. *Parallel Computation of Supersonic Reactive Flows with Detailed Chemistry Including Viscous and Species Diffusion Effects*. PhD thesis, Princeton U., 1997.

[34] W. Gropp, E. Lusk, and A. Skjellum. *Using MPI*. MIT Press, 1999.

[35] A. J. Kelly and R. G. Jahn. Pulsed electromagnetic acceleration: JPL contract no.954997. *MAE Report*, 1692.23, 1986.

[36] E.Y. Choueiri. The scaling of thrust in self-field MPD thrusters. *J. Prop. Power*, 14(5):744–753, 1998.

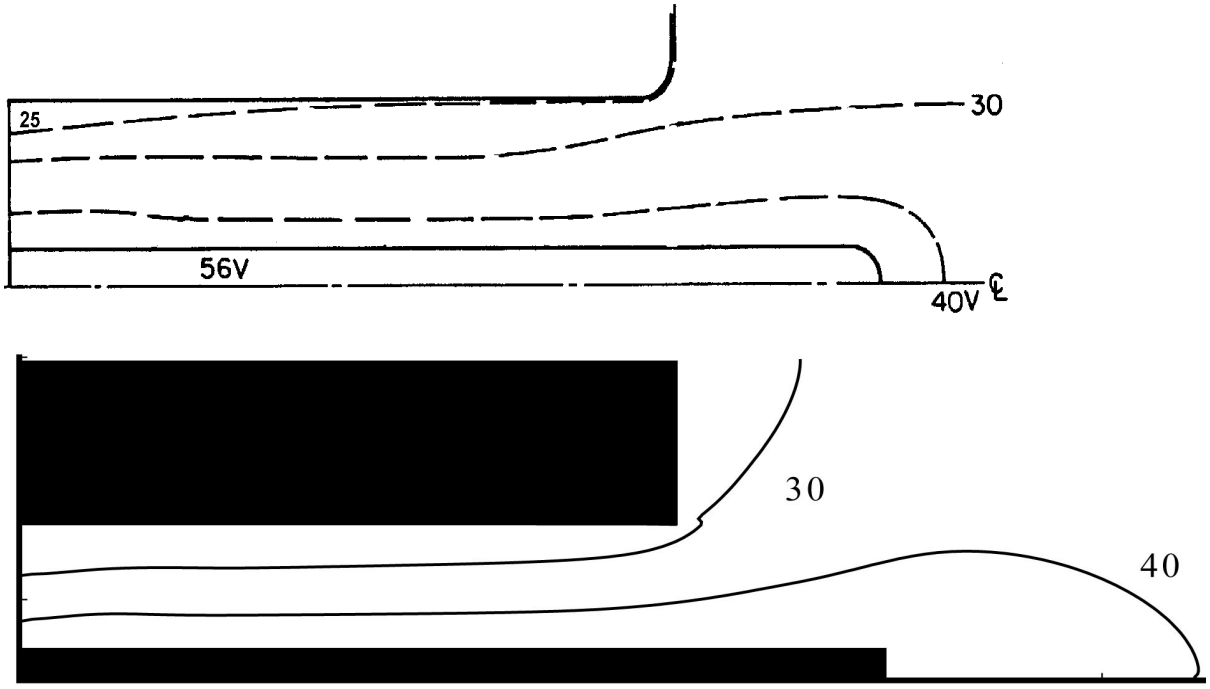

Figure 6: Measured (top) and calculated (bottom) potential contours

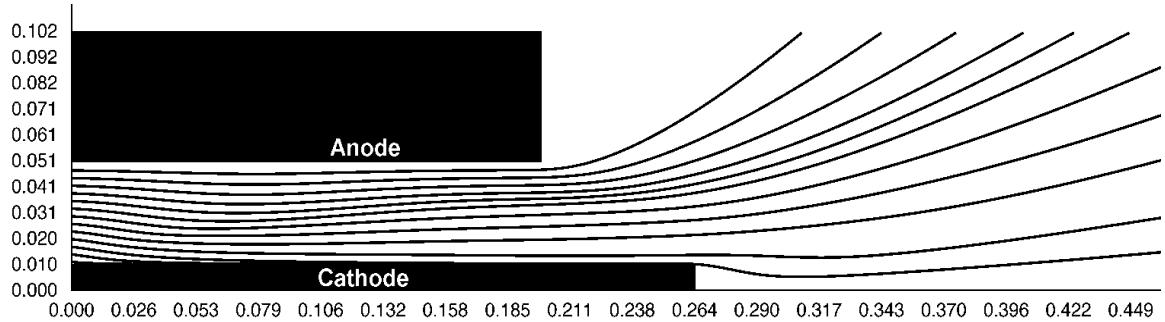

Figure 7: Velocity stream lines in the flow for argon at $\dot{m}$=6.0 g/s, and J = 15.0 kA

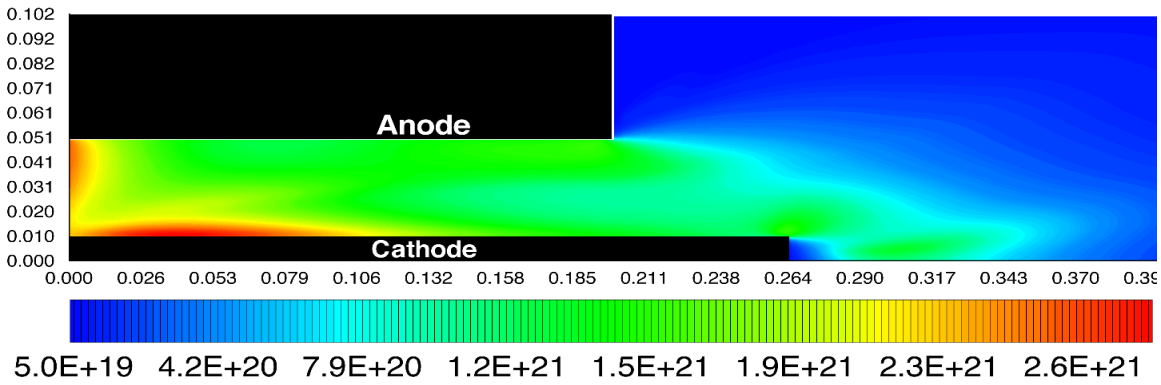

Figure 8: Distribution of electron number densities (in #/m^3) for argon at $\dot{m}$=6.0 g/s, and J = 15.0 kA

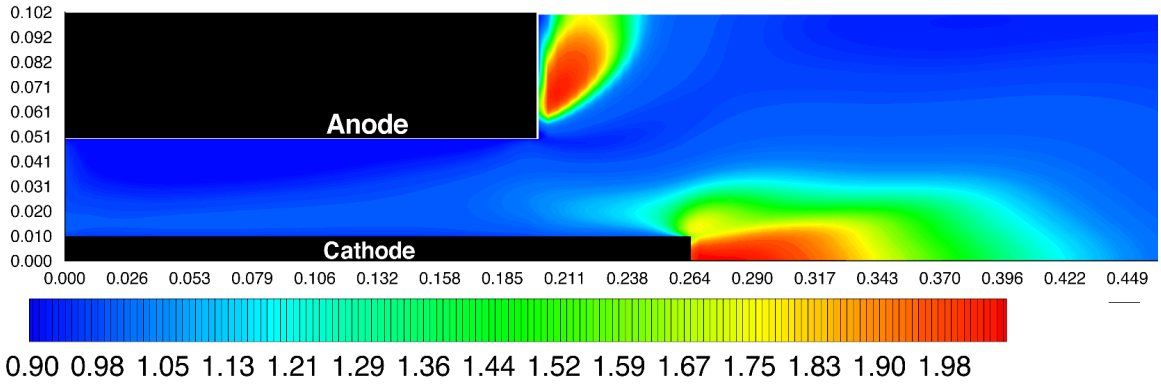

Figure 9: Distribution of ionization levels for argon at $\dot{m}$=6.0 g/s, and J = 15.0 kA

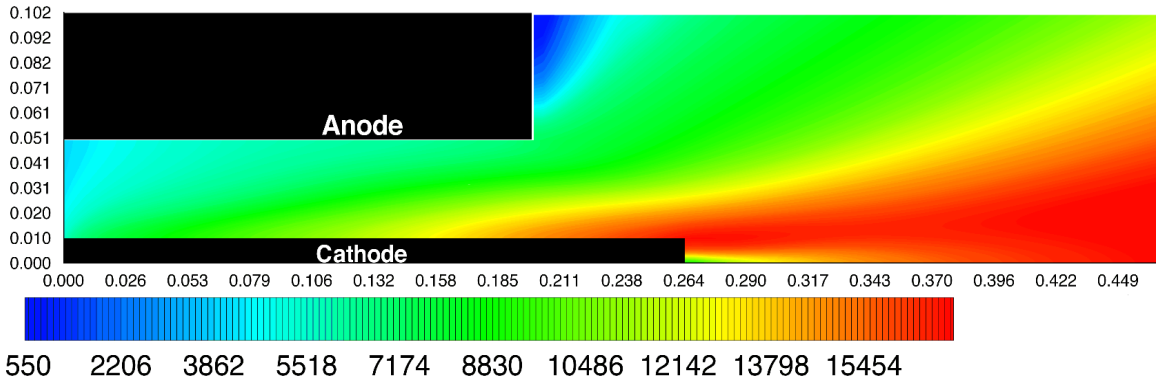

Figure 10: Distribution of axial velocities (in m/s) for argon at $\dot{m}$=6.0 g/s, and J = 15.0 kA